Growing Faults in the Lab: Insights into the Scale Dependence of the Fault Zone Evolution Process

Malte C. Ritter[1], Matthias Rosenau[1], Onno Oncken[1]

[1]Helmholtz Center Potsdam German Research Center for Geosciences GFZ, Potsdam, Germany

Key Points:

- Fault propagation work in sandbox models scales well with that in natural faults.
- The strain threshold for weakening to occur is scale-dependent.
- Diffuse deformation in sandbox models corresponds to the damage zone in natural faults.

Corresponding author: M. C. Ritter, `malte.ritter@gfz-potsdam.de`

Corresponding author: M. Rosenau, `rosen@gfz-potsdam.de`

Abstract

Analog sandbox experiments are a widely used method to investigate tectonic processes that cannot be resolved from natural data alone, such as strain localization and the formation of fault zones. Despite this, it is still unclear, to which extent the dynamics of strain localization and fault zone formation seen in sandbox experiments can be extrapolated to a natural prototype. Of paramount importance for dynamic similarity is the proper scaling of the work required to create the fault system, W_{prop}. Using analog sandbox experiments of strike-slip deformation, we show W_{prop} to scale approximately with the square of the fault system length, l, which is consistent with theory of fault growth in nature. Through quantitative measurements of both W_{prop} and strain distribution we are able to show that W_{prop} is mainly spent on diffuse deformation prior to localization, which we therefore regard as analogous to distributed deformation on small-scale faults below seismic resolution in natural fault networks. Finally, we compare our data to estimates of the work consumed by natural fault zones to verify that analog sandbox experiments scale properly with respect to energy, i. e. scale truly dynamically.

1 Introduction

Localization of strain into discrete shear zones and fault networks is a characteristic feature in the deformation of Earth materials on all scales from single grains to tectonic plates. In laboratory experiments on brittle rock the localization of strain into cracks and their subsequent coalescence to a through-going fracture are closely linked to a decrease of material strength known as strain weakening [*Brady et al.*, 1973; *Lockner et al.*, 1991; *Scholz*, 2002; *Paterson and Wong*, 2004]. On the larger scale of entire sedimentary basins strain localization can be observed as deformation being initially distributed onto several small faults and subsequently concentrating onto one master fault [e. g. *McLeod et al.*, 2000; *Cowie et al.*, 2005]. In the Andes, *Oncken et al.* [2012] were able to link this reduction of the number of active faults to a concurrent decrease of crustal strength. Their study uses field data to convincingly show the general behavior; however, the scarcity of geological data and the accuracy of available dating methods make it difficult to understand in detail the process of localization and its quantitative relation to strength evolution on various scales. Scaling laws have been employed to derive estimates regarding slip on faults below the resolution of a dataset [*Scholz and Cowie*, 1990], but their results remain untested.

Scaled analog sandbox experiments provide physical models in which the processes of interest can be observed directly and practically without limitations of resolution apart from the particle size of the selected material. Previous sandbox experiments focussing on strain localization have shown a phase of diffuse [*Adam et al.*, 2005] or ephemerally localized [*Dotare et al.*, 2016] deformation to precede formation of localized faults in sand. This can be linked to global material hardening [*Lohrmann et al.*, 2003; *Rechenmacher*, 2006] and is thus an essential part of the localization process [*Tordesillas and Muthuswamy*, 2009]. By analogy it has been related qualitatively to distributed deformation preceding localization in nature [e. g. *Dotare et al.*, 2016]. However, quantitative verification for this analogy is still missing.

In General, the applicability and extrapolation of the laboratory observations to nature usually relies on geometric, kinematic and dynamic similarity between the analog model and the natural prototype [*Hubbert*, 1937]. Similarity criteria include dimensionless numbers relating length, time and stress in the model and in nature and which should be the same in either setting. Rigorous dynamic similarity should result in proper scaling of energy, work, and eventually power. For a rate -independent deformation process as we consider here, kinematic scaling is arbitrary. Therefore, energy, or work, is the critical quantity to guarantee dynamic similarity.

Furthermore, the energy budget of the localization process has recently received increased attention due to its application in predicting fault growth through minimum-work models [*Mitra and Boyer*, 1986; *Hardy et al.*, 1998; *Masek and Duncan*, 1998; *Cooke and Murphy*, 2004; *Dempsey et al.*, 2012; *Cooke and Madden*, 2014]. In this context the work of fault propagation, W_{prop}, is recognized as the crucial parameter determining strain distribution and -localization [*Del Castello and Cooke*, 2007]. As usual in these studies, we define W_{prop} to be the work per unit height of the fault, where height refers to the in-plane extent of the fault perpendicular to the slip direction. The unit of W_{prop} is thus J m^{-1}. The common estimate used in all the above studies assumes W_{prop} to depend on the volume of the fault zone. Its width depends on the displacement on the fault [e. g. *Scholz*, 1987] and thus on fault length l [*Cowie and Scholz*, 1992; *Dawers et al.*, 1993]. This leads to the prediction of an overall scaling of fault zone volume, and thus W_{prop}, with l^2.

In contrast to this, shear zone width in granular media in general and in sandbox experiments in particular is depending on grain size and is otherwise constant [*Panien*

et al., 2006]. Accordingly, *Herbert et al.* [2015] have reported results from which W_{prop} can be deduced to be directly proportional to l, although this relationship was not in the focus of their study. If this linear relationship is valid, it carries severe implications for the applicability of sandbox experiments to understanding natural systems.

To resolve these issues we carried out a series of analog sandbox experiments varying the fault system length l systematically over a wide range. By quantifying diffuse deformation and W_{prop}, as well as their mutual relation, we show that diffuse deformation in sandbox experiments is analogous to distributed deformation in natural fault systems. Our data also verifies the dynamic similarity of sandbox experiments by means of scalability with respect to energy, i.e. it shows a similar scaling of W_{prop} with fault length as in nature.

2 Experimental Approach

In order to facilitate the formation of a sufficiently large fault system, we choose the tectonic setting of strike-slip deformation, in which l (defined here as the extent in slip direction) is not limited by crustal thickness. To further extend the range of l, we complement these experiments with measurements in a Ring-Shear tester that allows very precise measurements of forces for short l at the cost of not permitting direct observation of the shear zone.

2.1 Analog Material

The analog material used in this study is quartz sand of type G23T, which is the standard sand used for analog modeling at GFZ Potsdam. It is a medium-grained and moderately sorted fluvial sand with rounded grains (mean grain size $300\,\mu$m). Standard mechanical testing has been carried out on this sand by *Klinkmüller et al.* [2016]; *Ritter et al.* [2016], among others. The latter study found tectonic models using this material to be scaled most properly with respect to strength and strain weakening for a length scaling factor of $l^* = 2 \times 10^{-6}$, i.e. for the case of $1\,$cm in the model relating to $5\,$km in the natural prototype.

2.2 Deformation Rigs

2.2.1 Strike-Slip Shear Box

The strike-slip shear box is a custom built apparatus that is based on the deformation rig introduced in *Ritter et al.* [2017a]. It essentially consists of a sand pack, one part of which is pushed forward by a combination of an indenter and a moving sidewall, while the other part is held in place by a stationary back– and sidewall (fig. 1). The sand pack is resting on a layer of low-viscosity silicone oil that, in combination with a low deformation rate of $30\,\mu\mathrm{m\,s^{-1}}$, reduces the basal traction to approximately $10\,\mathrm{Pa}$. This is about $4\,\%$ of the average sand strength and thus enables the sand pack to be pushed forward as a whole without internal thrusting (average sand strength $\tau_\mathrm{prop} = 0.5\,\mu\sigma_\mathrm{n} = 0.5\,\rho g h \mu \approx 255\,\mathrm{Pa}$). A strike-slip shear zone develops between the edges of the indenter and the stationary back-wall. The force required to push the indenter forward is measured by a sensor attached to it (sampling rate: $1\,\mathrm{kHz}$), and a digital camera captures images of the sand pack's surface (recording rate: $1\,\mathrm{Hz}$), from which the surface deformation field is calculated by means of DIC (Digital Image Correlation).

The fundamental novelty of this shear box is the total absence of any pre-existing basal shear boundary condition, either distributed or discrete, which distinguishes it from the typical Riedel-type shear box and its derivates [*Dooley and Schreurs*, 2012]. Such basal shear zone would result in mode-III deformation of the sand pack and vertical propagation of the already localized basal shear zone. Here only the starting and ending points are given as stress singularities, between which a fault can freely develop. This leads to mode-II deformation and does not prescribe localization away from the end points.

In all strike-slip experiments presented here the sand pack is $50\,\mathrm{mm}$ high and $750\,\mathrm{mm}$ wide. The sand is sifted into the box to ensure a reproducibly high density, and it is levelled by carefully scraping off the topmost approximately $1\,\mathrm{mm}$ to a uniform height. The variable parameter is the initial distance between indenter and stationary back-wall, which is the fault system length l. It is set to $l = 200\,\mathrm{mm}$, $l = 300\,\mathrm{mm}$ and $l = 400\,\mathrm{mm}$ in this study.
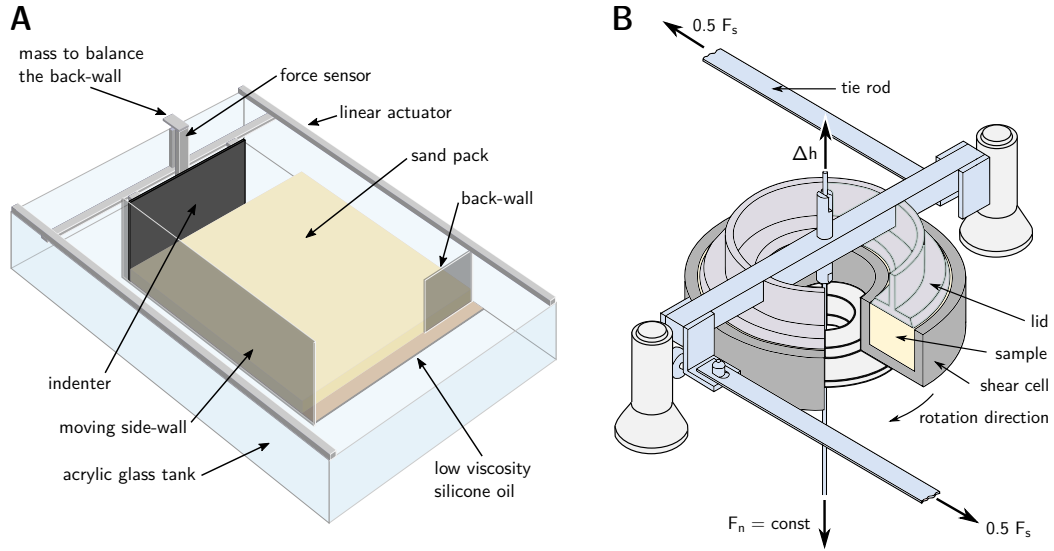
Figure 1. **A:** Experimental set-up for strike-slip experiments (SL). The sand pack is pushed by the indenter moving at a constant velocity. Due to a layer of low viscosity silicone oil the drag at the base of the sand pack is very small ($\approx 10\,\mathrm{Pa}$), such that when pushed the sand pack moves as a whole. A stationary back-wall holds back a part of the sand pack, which causes a shear zone to develop between the edges of the indenter and the back-wall. The parameters recorded are the force needed to push the indenter and its displacement. Additionally, a stereoscopic camera system (not shown) mounted above the set-up monitors the surface deformation of the sand pack. **B:** Experimental set-up for ring-shear tests (RST). The sample is sifted into the shear cell, which is then covered with the lid. A constant normal load is applied to the lid and the shear cell is rotated at a constant angular velocity, while the lid is kept stationary by tie rods. Radial vertical blades at the base of the lid (not shown) ensure mechanical coupling between lid and sample. The spacing l of these blades is varied between experiments. Sensors register the shear force F_s, the normal load F_n and the decompaction of the sample Δh. Modified from *Schulze* [1994].

2.2.2 Ring-Shear Tester

In order to extend the range of l towards lower values ($\leq 100\,\text{mm}$) we carry out complementary experiments in a ring-shear tester (RST). The RST is an industrial standard device (model *RST-01.pc*, manufactured by *Dr.-Ing. Dietmar Schulze Schüttgutmesstechnik, Wolfenbüttel*, Germany) that has already been used in several other studies in the analog modeling community [e. g. *Lohrmann et al.*, 2003; *Panien et al.*, 2006; *Klinkmüller et al.*, 2016; *Ritter et al.*, 2016; *Rosenau et al.*, 2017]. It was first introduced by *Schulze* [1994]. The RST consists of an annular shear cell and a matching lid between which the sample is contained. The shear cell is 40 mm high; it has an inner radius of 50 mm and an outer radius of 100 mm. The lid is pressed onto the sample at a preset normal load, σ_n. The shear cell is then rotated (angular velocity $\omega = 0.39\,\text{rad}\,\text{s}^{-1}$, corresponding to an average shearing velocity $v = 0.5\,\text{mm}\,\text{s}^{-1}$) while the lid is kept stationary by tie rods (fig. 1). Thereby the sample is sheared. Sensors record the torque and the normal load applied to the lid, as well as its vertical displacement due to volume changes of the sample.

The lid is equipped with small radial blades pointing vertically downwards from its base to provide sufficient mechanical coupling with the sample. These blades are 5 mm high and extend over the whole width of the ring. Upon rotating the shear cell, shear zones will nucleate at the tip of each of these blades and propagate towards the respective next one. The distance between two such blades is therefore the equivalent to the fault system length l in the strike-slip set-up and the parameter we vary in this study. We define the average circumferential distance between two blades as the distance along the imaginary circumferential line that separates the surface of the lid into two parts of equal area. For the sake of simplicity we will call this the "blade distance" from here on.

In the standard configuration of the lid there are 20 blades ($l = 24.4\,\text{mm}$). From this configuration blades were removed systematically, to realize blade distances of $l = 48.8\,\text{mm}$ (10 blades) and $l = 97.6\,\text{mm}$ (5 blades). Samples are sifted into the shear cell and then scraped off to the correct height.

2.2.3 Kinematic and Mechanical Differences Between the Set-Ups

Deformation in the two experimental set-ups is different to some degree: In the strike-slip box, normal load across the shear zone is due to lithostatic load, which increases from 0 Pa at the surface to approximately 850 Pa at the bottom of the sand pack.

Thus, there is a gradient of normal load across the fault from the surface to the bottom. At the same time, the slip rate is constant over the entire height of the sand pack. This is exactly opposite in the RST, where a constant normal load of $500\,\text{Pa}$ is applied on the entire fault surface by the lid, while the slip rate increases outwards by a factor of two, due to constant angular velocity. Although deformation of sand follows a velocity-independent rheology [*Rosenau et al.*, 2017], the velocity gradient causes a displacement gradient, which leads to slightly diachronous material failure with a circular failure front moving through the material from the periphery inwards. This is likely to flatten the force peak (lowering and widening). However, this does not change the area below the force curve and therefore does not bias the work inferred. The gradient of normal load, on the other hand, has a direct influence on fault strength, which in this case increases with depth. As the relationship between normal load and strength is linear, average values for normal loads, strengths and forces should nonetheless be reasonably good quasi-2D representations of the actual processes.

2.3 Work of Fault Propagation

According to *Herbert et al.* [2015] the total work balance for analog sandbox experiments is:

$$W_{\text{ext}} = W_{\text{prop}} + W_{\text{fric}} + W_{\text{grav}}. \tag{1}$$

W_{ext} is the external work done on the system, W_{fric} is the frictional work along the established (localized) shear zone and W_{grav} is the work done against gravity. In the case of strike-slip deformation the vertical component of deformation is negligible, such that $W_{\text{grav}} \approx 0$ in our models. The remaining parameters can be easily determined from the experiments: Measurements of bulk shear force in either experiment yield shear curves (fig. 2), that reveal a hardening – weakening cycle during deformation. According to *Lohrmann et al.* [2003], this is associated to a compaction – dilation cycle. Based on the micro-mechanical model of *Tordesillas and Muthuswamy* [2009] we suggest the onset of dilation to be equivalent to the onset of localization. As can be seen from the figure, this coincides with the onset of hardening. We therefore define the work of fault propagation W_{prop} as the area beneath the hardening – weakening peak, and the work done in frictional sliding on the shear zone W_{fric} as the remaining area under the shear curve. Both values are normalized to fault height. Note that our definition of W_{prop} is slightly different from other
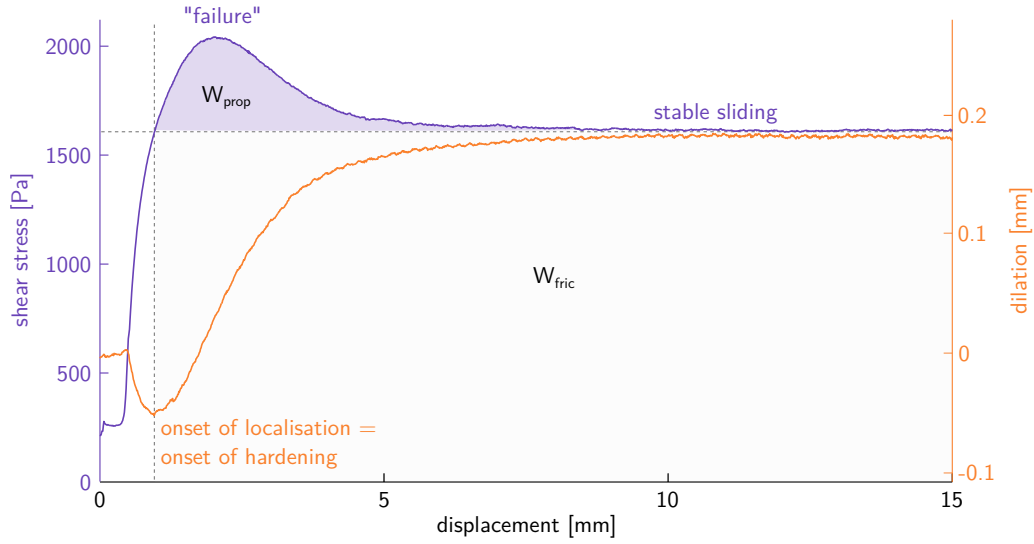
Figure 2. Shear stress and (blue) and sample dilation (orange) in a ring-shear experiment at σ_n = 3 kPa. Shear stress increases towards a maximum ("failure") and then decreases ("weakening") again towards a stable sliding stress. At the same time dilation takes place, which can be taken as a proxy for localization. The work required for fault propagation (W_{prop}) is defined as the area under the hardening – weakening peak, as shown by the blue-shaded area, and normalized to fault height. W_{fric} is the work for continued frictional sliding on the fault, which is the area under the shear stress curve that does not belong to W_{prop}, as indicated by the grey shading.

definitions that can be found in literature, which usually exclude the period of hardening prior to the force maximum [e. g. *Cooke and Madden*, 2014; *Herbert et al.*, 2015].

3 Results

3.1 Surface Deformation: Diffuse versus Localized Deformation

In the strike-slip set-up a total of nine experiments were carried out for different l. Surface displacement fields derived from DIC are used to analyse the fault evolution in these experiments. Fig. 3 exemplarily shows maps of the curl of the incremental displacement field for a representative experiment with l = 300 mm. The general pattern described in this example is independent of l in all experiments, as shown later.

In the beginning, deformation is diffuse and widely distributed in a sigmoidal patch between the edges of back-wall and indenter. Directly at the edges, however, it becomes
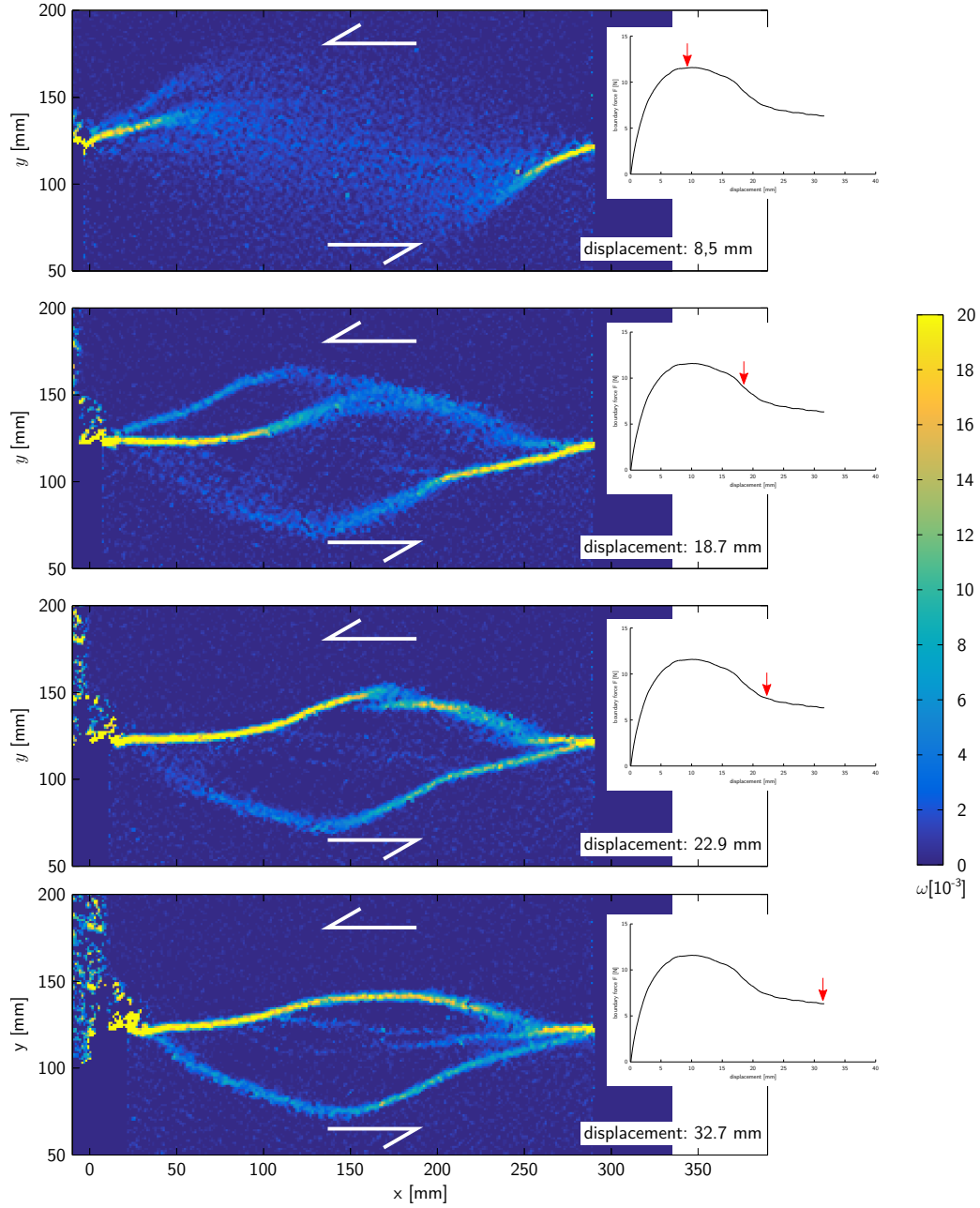
Figure 3. Evolution of a shear zone in strike-slip experiments, $l = 300\,\text{mm}$. Data shown is the curl of the incremental displacement field. The shear zones evolve in a complex pattern until finally an approximately straight shear zone is formed. See text for detailed analysis.

quickly, i.e. within a few millimeters of indenter displacement, localized into narrow shear zones that are a few centimetres long. They are rotated about 25° to 30° outwards with respect to the trace of the ideal, i.e. direct, connection between the edges of indenter and back-wall. This corresponds to the angle predicted by the Mohr-Coulomb failure criterion, if one assumes the pushing direction to be equal to the direction of maximum compressive stress. In the gap between the two shear zones deformation remains diffuse.

After accumulating some more displacement (about 5 mm) without growing significantly, the two initial shear zones become replaced by new ones that are oriented closer to the direction of imposed deformation; however, their tips are still bending outwards and away from each other (fig. 3). The new shear zones grow in a step-wise manner and eventually become replaced by a new, even more favorably oriented one. Before a new shear zone takes over the deformation, both shear zones, new and old, show simultaneous activity for a short time span.

In this way the shear zones grow towards and around each other until they eventually connect. When they finally do so, they connect not to the other fault's tip but somewhere close to its starting point, such that there are two adjacent fault branches, both connecting back-wall and indenter. In between the two branches, slight uplift (a few millimeters) can be observed. Activity then usually ceases on the more curved branch such that one main shear zone remains. It might straighten out slightly, but apart from that, deformation appears to have reached a steady state at this point.

To compare the evolution of experiments with different l, the cumulative displacement fields at the end of the experiments are used. Fig. 4 shows maps of their curl for one experiment of each l. It is clear from the figures that the general behavior of fault growth is the same independent of l: In all cases there are several distinct, abandoned shear zones at decreasing angles towards the deformation direction, and two main branches that connect to the other side. Due to the maps showing the cumulative deformation, the main shear zone at the end of the experiment cannot be clearly identified from the figure. This is only possible in the case of $l = 200\,\text{mm}$ (bottom), where an additional straight and through-going shear zone forms in the center.

To quantify the extent of diffuse and localized deformation, we measure the deformed area by counting the number of pixels that have undergone measurable deformation. We use the second component of the displacement gradient tensor ($\frac{\partial u_x}{\partial y}$, where u_x is
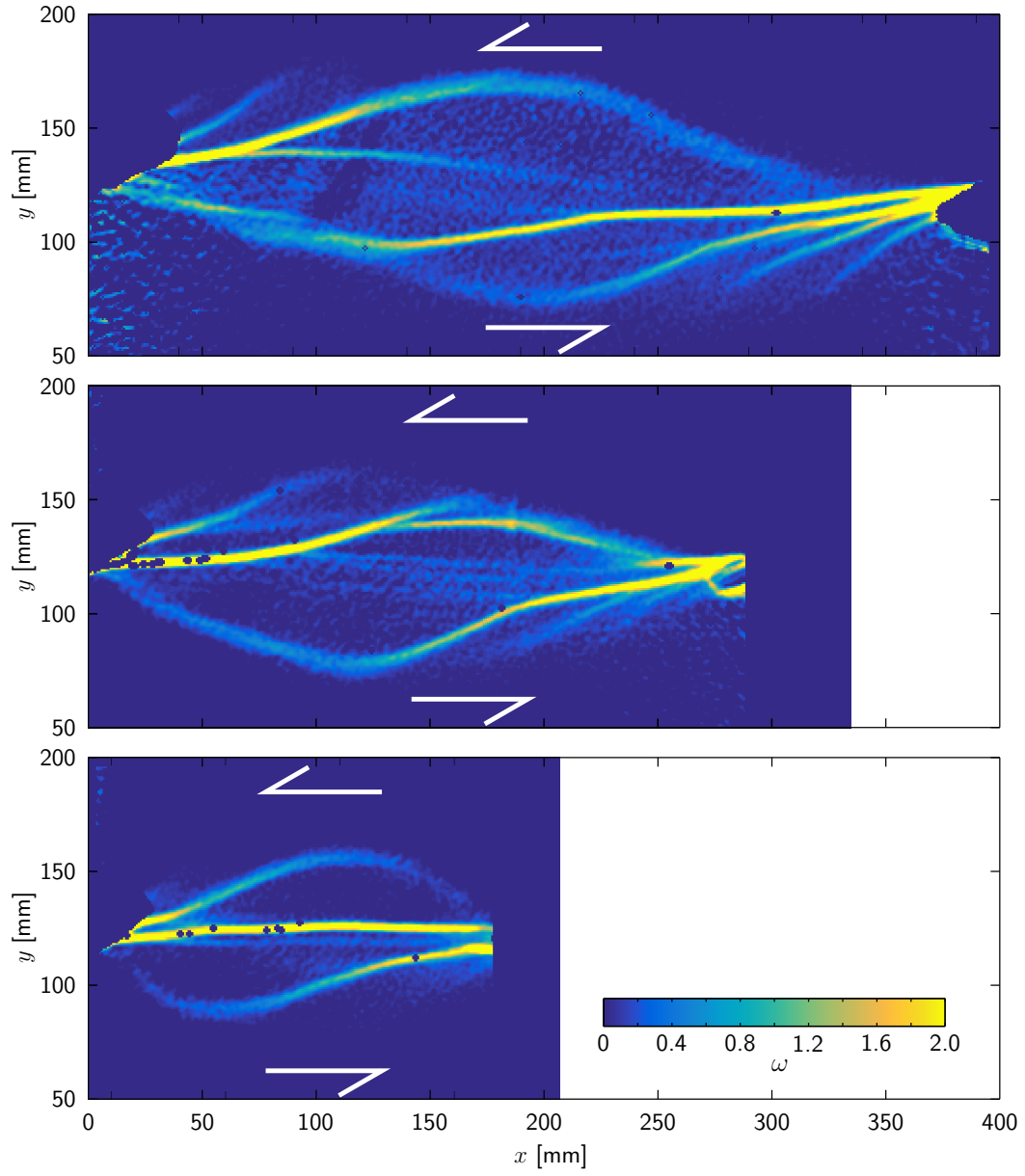
Figure 4. Maps of curl of cumulative displacement fields comparing experiments with different l. The overall structure is similar with shear zones curving around each other. However, the number of abandoned shorter shear zones and the amount of diffuse deformation increase significantly with l.

displacement along strike and y is in the direction perpendicular to it) and apply the algorithm of *Otsu* [1979] to find the best threshold between noise and measurably deformed area. This algorithm is designed to extract features from their background in an image based on intensity histograms. Because this relies on relative intensity differences, we are able to either include or exclude diffuse deformation in the pixel counting by applying the algorithm to displacement fields at two different, well-defined points during deformation: At peak stress practically no localized deformation has taken place yet. The algorithm thus finds a threshold that separates diffuse deformation from noise. This threshold can subsequently be applied to the final time step to measure overall diffuse deformation during the experiment. Applying the algorithm directly to the final time step, on the other hand, returns a threshold that retains only localized deformation. This is due to the fact that the intensity difference between distributed and localized deformation is much larger than between distributed deformation and noise. We are thus able to measure total deformation (of which localized deformation is only a minor fraction) and localized deformation separately.

Assuming plane strain deformation, the number of pixels displaying deformation can be transformed to the total volume V that has undergone deformation at any time during the experiment. Fig. 5 shows V normalized by l as a function of l. Without diffuse deformation, the volume per fault length (V_{loc}) is approximately constant. If, on the other hand, diffuse deformation is included, the volume per fault length (V_{diff}) increases overproportionately with l.

Fig. 6 shows along-strike profiles of distributed, cumulative slip for each experiment. These profiles are compiled by first masking out (i.e. setting to zero) areas of localized deformation and then summing up in y-direction all values $\frac{\partial u_x}{\partial y}$. The profiles show a maximum in the center of the shear zones, which is in accordance with the propagation of localization described above. Their maxima are slightly below the displacements required for formation of a through-going fault zone in the respective experiments, and correspond to the displacements at which weakening is complete (see below). When normalizing both the position along strike and the displacement to l, the profiles show a good data collapse, with the maximum distributed slip in the center of the shear zone being about 6 % of the fault length.
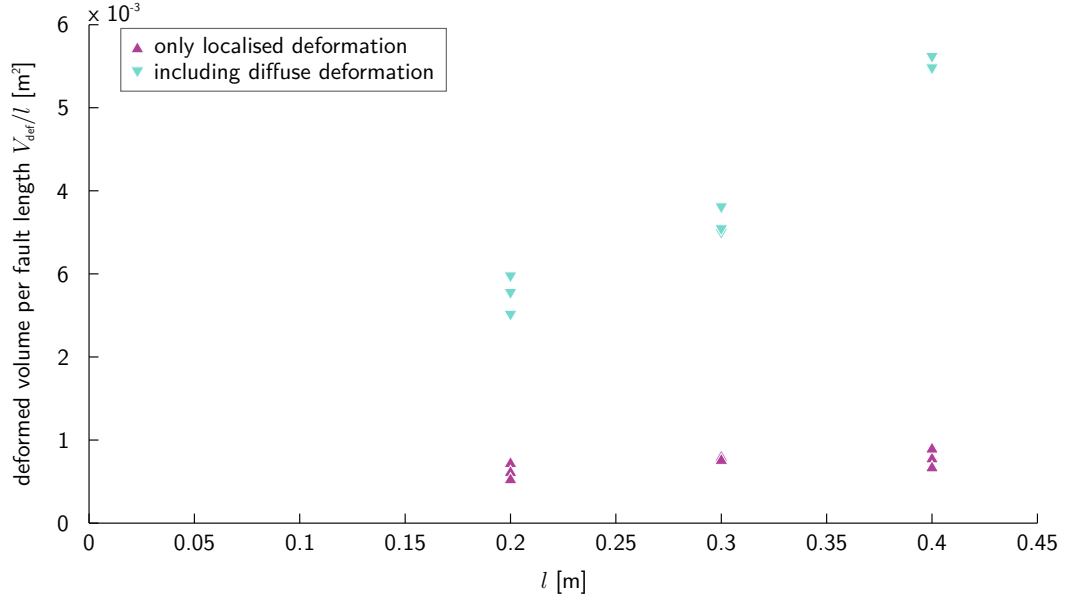
Figure 5. Deformed volume normalized to fault length in strike-slip experiments. The volume of the localized deformation is approximately constant, whereas the total volume including diffuse deformation shows a more-than-linear increase with l.
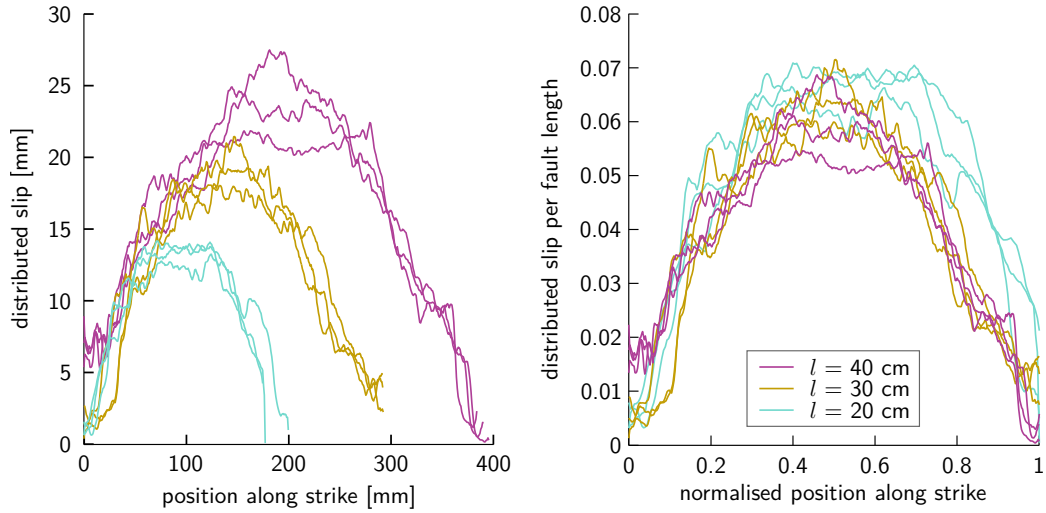
Figure 6. Distributed slip profiles for the strike-slip experiments. The profiles show a maximum in the center that corresponds to the amount of slip accumulated before weakening. Normalizing both axes to fault length results in a collapse of all experiments to one profile line with a maximum at about 6 % of the fault length.
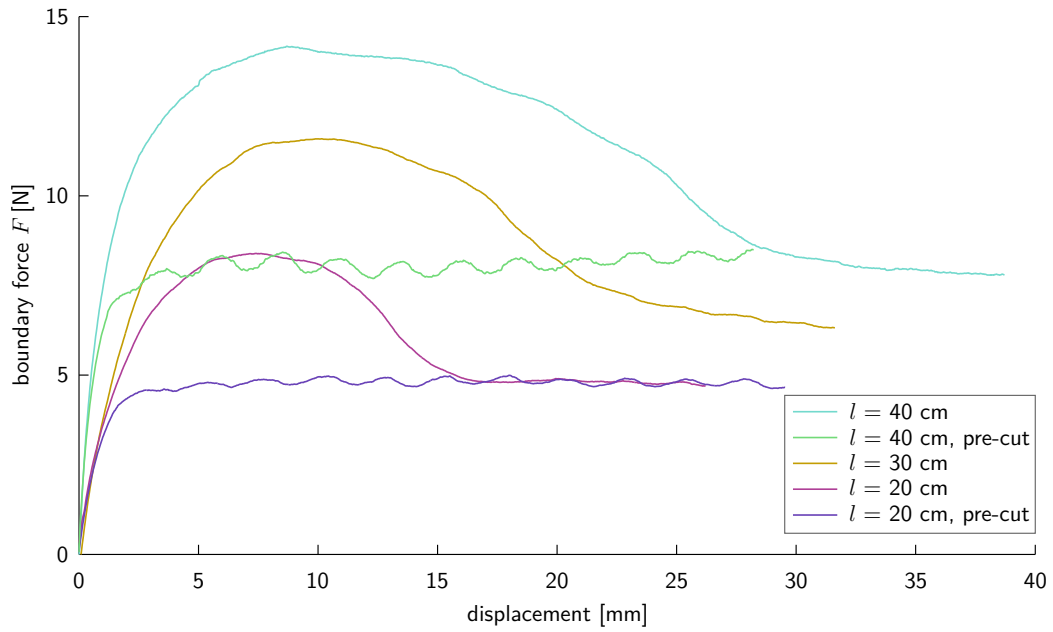
Figure 7. Boundary force vs. displacement in strike-slip experiments for different shear zone lengths l. Both peak and stable sliding force increase with l, which can be explained by an increased shear zone area. Reference measurements with a pre-cut sand pack were carried out for $l = 200$ mm and $l = 400$ mm. They do not exhibit any hardening – weakening behavior, but begin directly in the regime of stable sliding. The oscillatory pattern in these curves is probably due to the limited mechanical accuracy of the ball screws driving the deformation. The oscillation frequency corresponds to the angular frequency of the ball screws.

3.2 Driving Forces: Strain Hardening – Weakening and Work Budget

In the strike-slip set-up the pushing force was measured in all nine experiments. Fig. 7 exemplarily shows the shear force (corrected for basal drag) for one experiment of each l. The general behavior is similar for each of them: The curves show a hardening – weakening peak followed by a stable sliding phase in the end. Both peak height and stable sliding force increase with l, in accordance with an increasing fault surface area. The amount of displacement needed to achieve stable sliding increases with l, too, from approximately 15 mm for $l = 200$ mm to 30 mm for $l = 400$ mm (cf. fig. 6).

In addition to the experiments with undisturbed sand packs, experiments with a pre-cut shear zone were carried out for $l = 400$ mm and $l = 200$ mm. As shown in fig. 7, they do not exhibit hardening – weakening, but, after an initial increase, directly start into the regime of stable sliding that in the undisturbed experiments was attained after weakening.
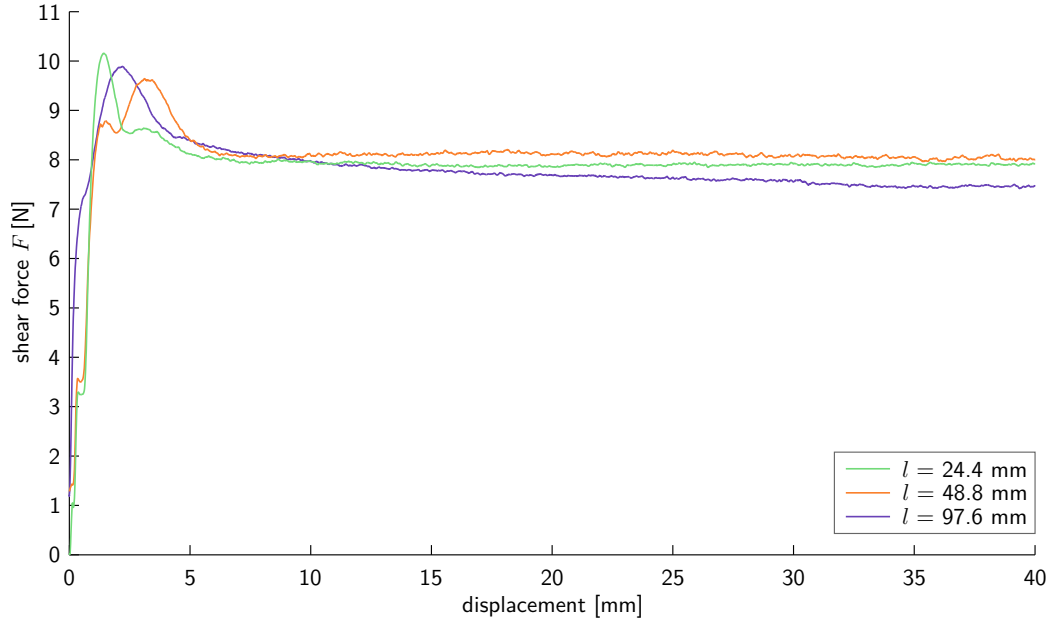
Figure 8. Shear curves from RST experiments for different shear zone lengths l. Peak and stable sliding strength are similar for all curves, but the peak width changes with l. All measurements carried out at $\sigma_n = 500\,\mathrm{Pa}$. All measurements are for total force at the sensors, i. e. integrated over all fault systems.

The force in these experiments shows a cyclic variation of maximally $\pm 0.5\,\mathrm{N}$ which is considered an artifact. It reflects the limited precision of the ball screws used to drive the deformation (repeat accuracy $\pm 0.02\,\mathrm{mm}$). The frequency of the variation corresponds to the angular frequency of the ball screws. The average level of the force is very similar to the stable sliding force at the end of the undisturbed experiments.

In the RST five independent measurements were carried out for each blade configuration. The normal load was set to $\sigma_n = 500\,\mathrm{Pa}$, which corresponds roughly to the average overburden load in the center of a 5 cm thick layer of sand, as used in the strike-slip experiments. Fig. 8 shows one example of a shear curve for each blade configuration. The measurements are the total force at the sensors, which is integrated over the number of fault systems created, i. e. the number of blades. As the final fault surface area is the same in all experiments independent of blade configuration, all three curves show almost identical stable shear forces and similar peak heights. The peak width, however, measured to the point where the shear force reaches a stable value, increases with blade distance, similar to what we observe in the strike-slip experiments.
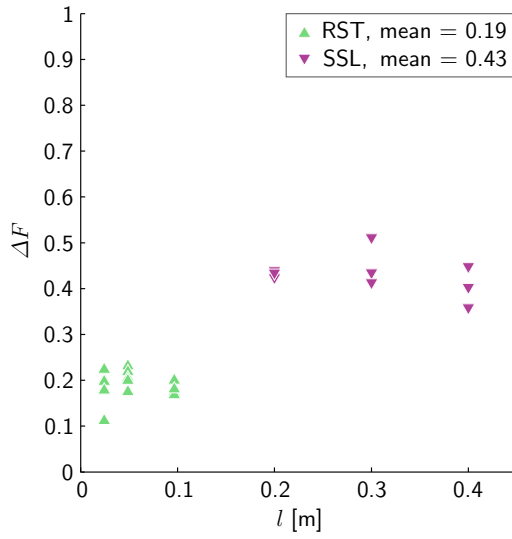
Figure 9. Relative weakening in the strike-slip (SSL) is about twice as much as in the RST. Within the respective set-ups it is independent of l.

To compare the weakening during fault formation for the different fault areas that occur in the two set-ups, we define the relative weakening in terms of force, ΔF:

$$\Delta F = 1 - \frac{F_\text{s}}{F_\text{p}} \tag{2}$$

where F_p and F_s are the maximum of the stress curve ("peak") and the subsequent plateau value ("stable"), respectively. ΔF will be between zero (no force drop, i.e. no peak) and one (drop to zero after the maximum). It is shown in fig. 9 for all experiments of either set-up. The figure clearly demonstrates that ΔF is independent of l, but differs between the two set-ups, being on average 0.19 in the RST and 0.43 in the strike-slip. This difference of approximately a factor of two is is due to the different ways shear zones are induced in the two set-ups: In the RST, stress concentrations at the tip of each blade initiate one fault per blade. These faults propagate in the direction of shear (i.e. rotation) until they meet the faults initiated at the respective next blade. Consequently, there is only one fault evolving per fault system, with the number of blades being equal to the number of fault systems. This is sketched in fig. 10.

In the strike-slip experiments, on the other hand, two faults evolve in one fault system, one initiating at either side of the set-up (figs. 3 and 10). They evolve in parallel and overlap until finally one of the two faults is abandoned. The total area of the fault planes is hence twice as large as it would be in the RST for the same l, which for a given ma-
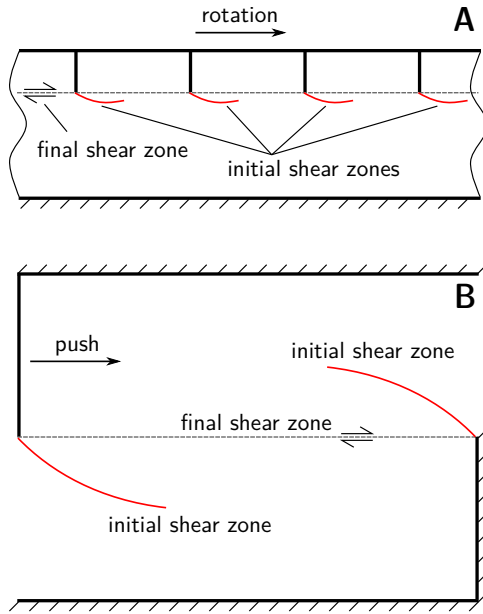
–17–

Figure 10. Conceptual sketch of shear zone formation in the two different set-ups.

A: Section of the Ring-shear tester. One shear zone forms at the tip of each blade and propagates in rotation direction towards the next blade. The fault system under consideration extents from one blade towards the next; several fault systems develop simultaneously.

B: Strike-silp set-up. Only one fault system develops, that contains two faults. The work required to deform this fault system on a given scale is twice as much as in the RST. Sketches are not to scale.
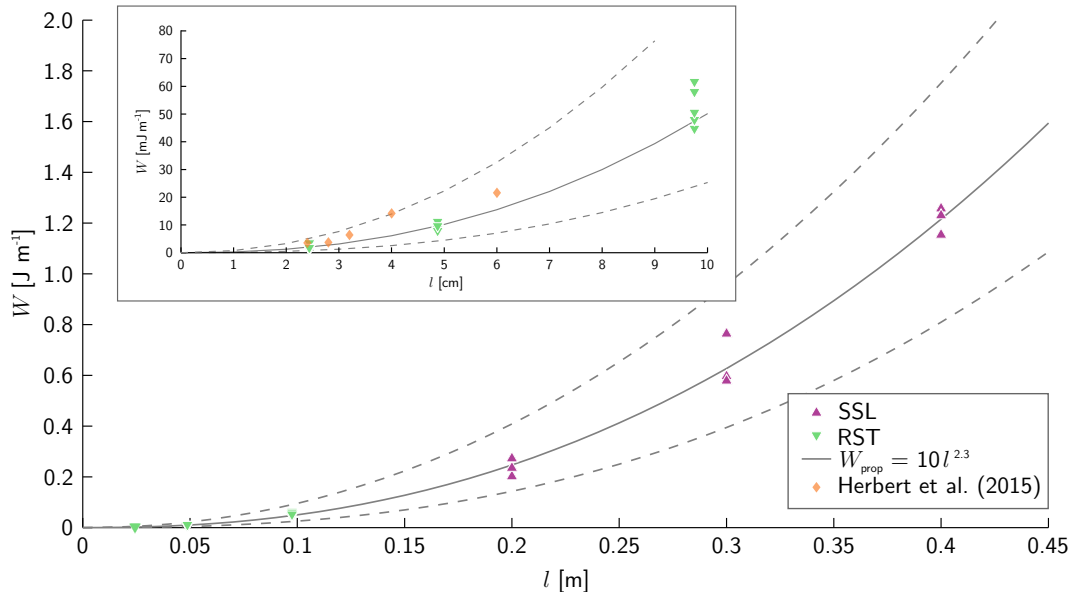
Figure 11. Work required for propagation of a single fault in Ring-Shear tests (inset shows a close-up) and strike-slip experiments increases overproportionately with fault system length l. The grey lines show a power-law fit to the data (solid) and its error (dashed). Data from *Herbert et al.* [2015] are shown for comparison.

terial strength results in the force being twice as high, too. This changes towards the end of an experiment when one of the fault branches is abandoned. Consequently, the stable sliding force is the same as it would be in the RST for the respective l, and thus the weakening is twice as high.

From the shear curves the work for fault propagation W_{prop} is determined: The transition from weakening to stable sliding is picked by hand in each shear curve and the area under the thus confined peak is measured (see definition in fig. 2). The values obtained in this way represent the formation of two faults in case of the strike-slip experiments, and of a variable number of faults depending on blade configuration in case of the RST (see above). Therefore, all measurements from the strike-slip experiments are divided by two, and all measurements form the RST are divided by the number of blades in the respective experiment, before being normalized to fault height. The resulting W_{prop} as a function of l is shown in fig. 11. The plot shows a strongly non-linear increase of W_{prop}, with values ranging from $1\,\mathrm{mJ\,m^{-1}}$ to $1260\,\mathrm{mJ\,m^{-1}}$ for the range of l covered by our data.

Fig. 12 shows W_{prop} normalized to the deformed surface area A. As W_{prop} is defined as work per height, dividing by the surface area effectively results in a work per volume.
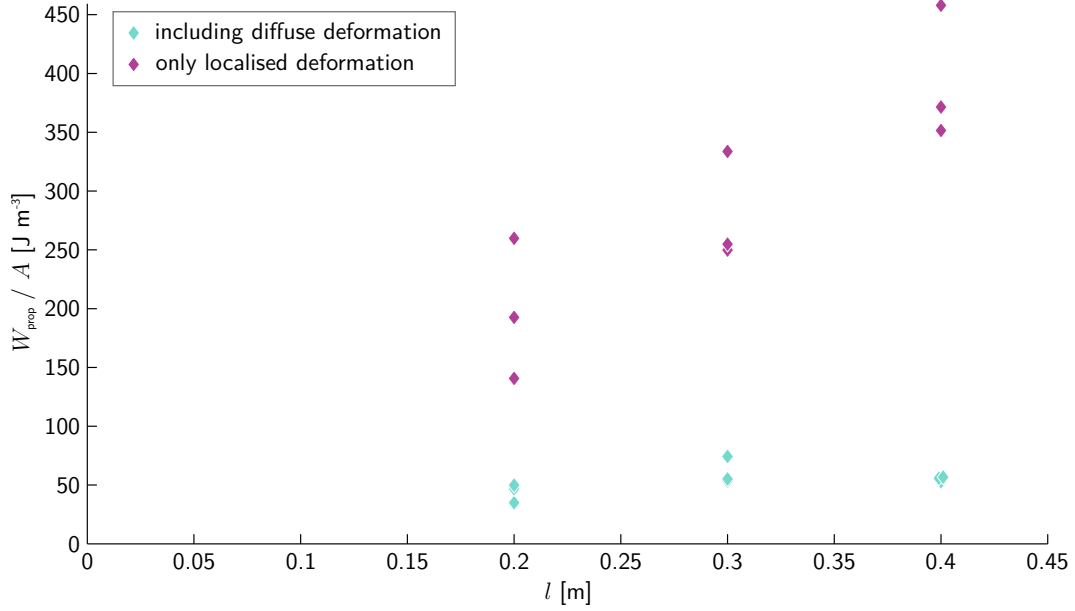
Figure 12. W_{prop} normalized to the surface area of the localized shear zone increases linearly with fault length l, while it is constant at $55\,\mathrm{J\,m^{-3}}$, if diffuse deformation is included into the surface area.

It increases with l, if $A = A_{loc}$ i.e. only localized deformation is taken into account. If the total diffuse deformation is considered as well ($A = A_{diff}$), the work per volume is constant and about $55\,\mathrm{J\,m^{-3}}$.

4 Discussion

4.1 Assessing the Complementarity of the Two Set-Ups

Optical monitoring of the strike-slip experiments shows that the final shear zone is often curved; thus it often deviates from the shortest possible fault path which might be considered the energetically preferred one. Hence it is conceivable that the evolution of the shear zone at the end of our experiments is not in a stable state yet, and more weakening might be possible. In this case ΔF and W_{prop} determined in our experiments would underestimate the true values. However, the average level of shearing force in the experiments with pre-cut, straight shear zones is similar to the stable sliding force in the experiments with undisturbed sand packs. From this we conclude that, despite the shear zones still being curved, weakening is largely complete at the end of an experiment and our estimates for ΔF and W_{prop} are good representations of the true values.

Furthermore, we have set the normal load in the RST-experiments to $\sigma_\mathrm{n} = 500\,\mathrm{Pa}$, which equals the overburden pressure in the center of an approx. $5\,\mathrm{cm}$ thick sand pack. By comparing the result of RST and strike-slip experiments we have implicitly assumed that this overburden load reflects the normal load on the shear zone, and that variations with depth cancel out in total. This assumption can be justified by comparing the stable sliding forces in the two set-ups: In either one, the RST and the strike-slip one (for $l = 40\,\mathrm{cm}$), stable sliding requires a force of approximately $7.9\,\mathrm{N}$. The fault area is $A_\mathrm{RST} = 226.19\,\mathrm{cm}^2$ for the RST and $A_\mathrm{SSL} = 200\,\mathrm{cm}^2$ for the strike-slip experiment. Stable sliding stress is thus slightly higher in the strike-slip case than in the RST, but the difference is still within the range of measurement variations of the strike-slip experiments. The two set-ups therefore can in fact be regarded as complementary with respect to the load conditions.

4.2 Interpretation at the Laboratory Scale

Our experiments show that in sand the work of fault propagation, W_prop, increases with fault length in a nonlinear way. In search for a law that describes both our data subsets, RST and strike-slip, with a common set of parameters, we find the closest fit with a function of the form

$$W_\mathrm{prop} = al^b. \tag{3}$$

Here, a and b are free parameters that we determine through least squares fitting. Doing so for both subsets individually returns similar values for a and b, respectively (tab. 1). A joint fit to the complete dataset ("combined" in tab. 1) yields the empirical relation for W_prop in sand under the given normal load conditions:

$$W_\mathrm{prop} = 10(2)\,\mathrm{J\,m}^{-1} \left(\frac{l}{l^\circ}\right)^{2.3(2)} \tag{4}$$

where l° is the unit length. This relation is also shown in fig. 11. The numbers given in parentheses are the numerical values of the uncertainty of the fit (95 %-interval of confidence) and referred to the corresponding last digit of the respective fit parameter. They do not include the accuracy of the measurements themselves. Considering the low number of experiments conducted, it is reasonable to assume that the total error might be larger. Our data therefore do not exclude a simple quadratic dependency. Nonetheless, they are in definite contrast with the interpretation of *Herbert et al.* [2015] that implies a linear relationship on l. This discrepancy probably stems from the fact that their study relies on a

Table 1. Parameter returned from fitting a function of the form $W_{\mathrm{prop}} = al^b$ to measurements of W_{prop}. The data were normalized to the number of faults and to fault heigh h prior to fitting. The numbers given in parentheses are the numerical values of the uncertainty of the fit (95 %-interval of confidence) and referred to the corresponding last digit of the respective fit parameter. See text for explanation.

	a (J m^{-1})	b
RST	19 (22)	2.3 (5)
strike-slip	10 (4)	2.3 (4)
combined	10 (2)	2.3 (2)

limited range of values for l, as it was not intended to test for a relationship of W_{prop} on l but focussed on normal load instead. They used a convergent wedge setting and varied the sand pack thickness from 12 mm to 20 mm to realize different normal load conditions. However, from the specifications of their experiments we are able to derive an approximate comparison of their data to ours: We transform the sand pack thicknesses to fault lengths (assuming a fault dip of 30°) and remove the normalization to fault length from their work data. The resulting data we project to a normal load of 500 Pa to make them comparable to our normal load conditions. The results of this projection are shown along with our RST-data in the inset in fig. 11. The two datasets show a good congruence which verifies the experimental approaches used in either study.

The good correlation between W_{prop} and A_{diff} that we observe in our data (fig. 12), supports our hypothesis of diffuse deformation being the main energy sink during fault formation in sand. As the width of the total area affected by deformation, i.e. the distance between the two outermost faults in the maps in fig. 4, is more or less constant, the total volume that is available for diffuse deformation increases only linearly with l. Nevertheless, the fraction of the volume that actually becomes deformed increases according to the above power-law, resulting in an increasing density of deformed pixels in the recordings. Consequently, the maximum shear strain the material in the deformed area undergoes prior to failure is not a material property, but depends on the size of the system. This is confirmed by the observation that failure on the system scale in all experiments occurs when the distributed slip has reached about 6 % of the fault system length. Taken together, this leads to the conclusion of the average rate of fault propagation being constant over the

range of l tested. We interpret this to be an indicator for localization to be at least partially driven by the kinematic boundary condition at the edges of indenter and back-wall.

4.3 Application to Natural Systems

4.3.1 Comparison of Work Estimates

Estimates of W_prop in natural rock are subject to large uncertainties, mainly because of the difficulty to directly measure it at the relevant scales. A common approach assumes W_prop to be the sum of the work done in creating the fault itself and the work done in creating a damage zone around it [*Mitra and Boyer*, 1986]:

$$W_\text{prop} = \gamma l + \gamma l r w \tag{5}$$

As all expressions for W_prop in this article, this is a two-dimensional, plane-strain formulation that implicitly assumes a unit length in the third dimension. γ is the surface energy per unit area, ranging from $10^1 \, \text{J m}^{-2}$ to $10^4 \, \text{J m}^{-2}$ for common rock-forming minerals [*Wong*, 1982; *Cox and Scholz*, 1988; *Del Castello and Cooke*, 2007]. l is the length over which the fault grows and r is the density of fractures in the damage zone around and ahead of the fault tip, which is around $500 \, \text{m}^{-1}$ according to *Mitra and Boyer* [1986]. w is the width of the damage zone that is 0.1 times to 0.01 times the fault displacement [*Scholz*, 1987]. This in turn is linearly related to l by some material constant c' [*Cowie and Scholz*, 1992; *Dawers et al.*, 1993], such that $w = c \, l$, where c is a material parameter of the order of 10^{-2} [*Scholz*, 2002]. Substituting w with $c \, l$ results in:

$$W_\text{prop} = \gamma \left(l + c r l^2 \right) \tag{6}$$

The quadratic term refers to the damage zone around the fault and the linear one to the fault itself. This dependence of the spatial dimension of the damage zone on l^2 is also in accordance with modern fracture mechanics [*Scholz*, 2002]. However, the linear term implies the fault to be a discrete, planar feature that forms in a separate process, which is probably not the case. Instead, most faults encompass a granulated core of finite width that forms by frictional wear from the intensely fractured material of the damage zone [e. g. *Scholz*, 2002]. This process occurs whenever a fault slips and does not cease after localization. Hence, we argue that formation of the fault core is not part of the localization process. A more accurate estimate of W_prop would thus omit the linear term in eq. 6 and rather include the formation of the fault core in W_fric instead. However, the

–23–

discrepancy between these two estimates is negligible; it is on the order of 0.1 % to 1 % for $l = 100$ m and quickly decreases for longer faults. Following this, we assume W_{prop} in nature to be a function of l^2 which is, within the range of measurement accuracy, similar to our experimentally found values for sandbox models.

Another approach to determine W_{prop} in nature is to measure the surface area created by a single earthquake, determine the surface energy spent, and sum this over the number of earthquakes experienced by the fault. For the 100 m long Bosman fault, South Africa, that formed in just one earthquake and was sampled immediately afterwards, *Wilson et al.* [2005] report the surface energy consumed to be in the range of approximately 3 MJ m^{-2} to 10 MJ m^{-2}. For the Punchbowl fault in the San Andreas system, California, *Chester et al.* [2005] determine the fracture surface energy per earthquake to be approximately 0.5 MJ m^{-2}. They estimate the total 44 km of displacement to have accumulated over about 10 000 earthquakes, which results in the total energy required for creation of a fault of comparable size to be 5×10^9 J m^{-2} to 10^{11} J m^{-2}. Assuming a fault length of 440 km [*Scholz*, 2002], eq. 6 results in values ranging from 2.2×10^7 J m^{-2} to 2.2×10^{10} J m^{-2} for the same situation.

Applying the scaling factors for sandbox models derived in *Ritter et al.* [2016] we determine a model fault length of 0.88 m to be analogous to this case. From eq. 4 this results in $W_{\text{prop}} = 8.47$ J m^{-2} in the model. The scaling factor for energy per area can be calculated as the product of the scaling factors for stress and length, $\sigma^* l^* = 2.42 \times 10^{-12}$ [*Ritter et al.*, 2016]. Scaling the model result up to nature with this factor yields $W_{\text{prop}} = 3.5 \times 10^{12}$ J m^{-2}. This is slightly higher than the values derived for natural faults above, but still acceptably close considering the uncertainty of four orders of magnitude for the natural estimates. Consequently, our results are also numerically similar to natural fault systems.

4.3.2 Analysis of Strain Distribution

We interpret the fault system evolving in our experiments as representing a transfer fault system linking two segments of dip-slip faults, where the two displacement singularities (indenter and back-wall) correspond to the edges of the dip-slip faults. This termination by conversion into a dip-slip fault is one of three geometrically possible terminations of a strike-slip fault [*Ramsay*, 1980; *Mouslopoulou et al.*, 2007]. Natural examples

include the Tjörnes Fracture zone in Iceland [*Gudmundsson*, 1995] and the Las Vegas Valley Shear Zone in Nevada [*Duebendorfer and Black*, 1992].

The pattern of overlap of the shear zones we observe in our experiments is similar to that in restraining double bends occurring in natural strike-slip shear zones [e. g. *Cunningham and Mann*, 2007]. The uplift we observe resembles – although negligibly small with respect to the work calculations – the pop-up or positive flower structure that usually can be found in natural structures in this context [*Cunningham and Mann*, 2007; *Cunningham*, 2007]. Commonly, natural restraining bends are interpreted to be related to inherited structures within the trace of a strike-slip shear zone, such as a step-over in a pre-existing basement fault [*Cunningham and Mann*, 2007]. Our results contrastingly suggest that an inherited structure is not a necessary condition; instead restraining bends seem to develop whenever two fault segments that follow the same fault trace approach each other. This is particularly well exemplified in fig. 4 for the case of $l = 30\,\text{cm}$, where the two segments first propagate directly towards each other before they turn outwards. We interpret this as being due to the stress distribution around each fault segment which makes it impossible for the segments to link directly tip to tip.

Furthermore, we observe a succession of short-lived shear zones that occur directly at the edges of indenter and back-wall during the hardening regime. They appear at decreasing angles with respect to the final fault trace, and their number is highest for long fault systems. Their initial orientation according to a Mohr-Coulomb failure criterion suggests that the first such shear zone represents the dynamically favored path. The final direction of the through-going shear zone, however, is strongly predetermined by the fixed kinematic boundary condition. We therefore interpret the succession of these shear zones as being the result of a competition between the dynamically preferred and the kinematically imposed shear zone direction. To our knowledge, similar shear zone patterns have not been reported from any natural fault system so far. This might be either due to lack of preservation of such features, or due to the edge of the dip-slip fault in nature being more compliant than the indenter in the experiment, resulting in a weaker kinematic boundary condition.

In natural basin-scale fault systems, the formation of a through-going, localized fault is preceded by deformation on multiple smaller-scale, but nevertheless localized faults [*McLeod et al.*, 2000; *Cowie et al.*, 2005]. This precursory fault network cannot be re-

solved as such in the sandbox. Instead, we regard the diffuse deformation observed in our experiments as analogous to this diffusely-localized fault network, since it is persistent plastic deformation which in brittle rock always takes the form of micro-cracks, fractures and faults. From our measurements of diffuse strain we interpret the density of such fracture networks to be a function of fault system size in nature, too. This carries implications for bulk rock permeability in sedimentary basins and reservoir rock affected by faulting, which are often controlled by fractures that are below seismic resolution. Our findings provide a relative scaling for such fracture systems based on system size. Additionally, such increase of fracture density away from the through-going fault is identical to a decrease of strain localization. Therefore, no unique quantitative relation between strain localization and the constant strain weakening can be formulated.

5 Conclusion

We have carried out analog sandbox experiments of strike-slip deformation in which we simultaneously monitored stress and strain. We find the work of fault propagation, W_{prop}, to be directly proportional to the volume of diffusely deformed material, V_{diff}, with a numerical value of about $55\,\mathrm{J\,m^{-3}}$. In contrast to earlier sandbox studies, but consistent with theory of fault growth in nature, both W_{prop} and V_{diff} show an approximately quadratic dependence on fault system size, while at the same time the total stress drop during localization is constant. Numerical values of W_{prop} scale well to estimates from natural fault zones. Additionally, our data for the first time show quantitatively that distributed deformation in sandbox models mimics natural damage zone evolution and can be interpreted as a proxy for deformation below seismic resolution in crustal-scale fault systems. We therefore support the traditional view of sandbox experiments being dynamically similar to their natural prototype.

The data used in this study are available from the supplementary data publication of *Ritter et al.* [2017b]

References

Adam, J., J. L. Urai, B. Wieneke, O. Oncken, K. Pfeiffer, N. Kukowski, J. Lohrmann, S. Hoth, W. van der Zee, and J. Schmatz (2005), Shear localisation and strain distribution during tectonic faultingâĂŤnew insights from granular-flow experiments and high-resolution optical image correlation techniques, *Journal of Structural Geology*, *27*(2), 283–301, doi:10.1016/j.jsg.2004.08.008.

Brady, B. T., W. I. Duvall, and F. G. Horino (1973), An experimental determination of the true uniaxial stress-strain behavior of brittle rock, *Rock Mechanics Felsmechanik Mécanique des Roches*, *5*(2), 107–120, doi:10.1007/BF01240161.

Chester, J. S., F. M. Chester, and A. K. Kronenberg (2005), Fracture surface energy of the Punchbowl fault, San Andreas system, *Nature*, *437*(7055), 133–136, doi:10.1038/nature03942.

Cooke, M. L., and E. H. Madden (2014), Is the Earth Lazy? A review of work minimization in fault evolution, *Journal of Structural Geology*, *66*, 334–346, doi:10.1016/j.jsg.2014.05.004.

Cooke, M. L., and S. Murphy (2004), Assessing the work budget and efficiency of fault systems using mechanical models, *Journal of Geophysical Research: Solid Earth*, *109*(B10), 1–13, doi:10.1029/2004JB002968.

Cowie, P. A., and C. H. Scholz (1992), Physical explanation for the displacement-length relationship of faults using a post-yield fracture mechanics model, *Journal of Structural Geology*, *14*(10), 1133–1148, doi:10.1016/0191-8141(92)90065-5.

Cowie, P. A., J. R. Underhill, M. D. Behn, J. Lin, and C. E. Gill (2005), Spatio-temporal evolution of strain accumulation derived from multi-scale observations of Late Jurassic rifting in the northern North Sea: A critical test of models for lithospheric extension, *Earth and Planetary Science Letters*, *234*(3-4), 401–419, doi:DOI 10.1016/j.epsl.2005.01.039.

Cox, S., and C. H. Scholz (1988), On the formation and growth of faults: an experimental study, *Journal of Structural Geology*, *10*(4), 413–430, doi:10.1016/0191-8141(88)90019-3.

Cunningham, D. (2007), Structural and topographic characteristics of restraining bend mountain ranges of the Altai, Gobi Altai and easternmost Tien Shan, *Geological Society, London, Special Publications*, *290*(1), 219–237, doi:10.1144/SP290.7.

Cunningham, W. D., and P. Mann (2007), Tectonics of strike-slip restraining and releasing bends, *Geological Society, London, Special Publications*, *290*(1), 1–12, doi:10.1144/SP290.1.

Dawers, N. H., M. H. Anders, and C. H. Scholz (1993), Growth of normal faults: Displacement-length scaling, *Geology*, *21*(12), 1107–1110, doi:10.1130/0091-7613(1993)021<1107:gonfdl>2.3.co;2.

Del Castello, M., and M. L. Cooke (2007), Underthrusting-accretion cycle: Work budget as revealed by the boundary element method, *Journal of Geophysical Research*, *112*(B12), B12,404, doi:10.1029/2007JB004997.

Dempsey, D., S. Ellis, R. Archer, and J. Rowland (2012), Energetics of normal earthquakes on dip-slip faults, *Geology*, *40*(3), 279–282, doi:10.1130/G32643.1.

Dooley, T. P., and G. Schreurs (2012), Analogue modelling of intraplate strike-slip tectonics: A review and new experimental results, *Tectonophysics*, *574-575*, 1–71, doi:10.1016/j.tecto.2012.05.030.

Dotare, T., Y. Yamada, J. Adam, T. Hori, and H. Sakaguchi (2016), Initiation of a thrust fault revealed by analog experiments, *Tectonophysics*, *684*, 148–156, doi:10.1016/j.tecto.2015.12.023.

Duebendorfer, E. M., and R. A. Black (1992), Kinematic role of transverse structures in continental extension: An example from the Las Vegas Valley shear zone, Nevada, *Geology*, *20*(12), 1107, doi:10.1130/0091-7613(1992)020<1107:KROTSI>2.3.CO;2.

Gudmundsson, A. (1995), Ocean-ridge discontinuities in Iceland, *Journal of the Geological Society*, *152*(6), 1011–1015, doi:10.1144/GSL.JGS.1995.152.01.22.

Hardy, S., C. Duncan, J. Masek, and D. Brown (1998), Minimum work, fault activity and the growth of critical wedges in fold and thrust belts, *Basin Research*, *10*(3), 365–373, doi:10.1046/j.1365-2117.1998.00073.x.

Herbert, J. W., M. L. Cooke, P. Souloumiac, E. H. Madden, B. C. Mary, and B. Maillot (2015), The work of fault growth in laboratory sandbox experiments, *Earth and Planetary Science Letters*, *432*, 95–102, doi:10.1016/j.epsl.2015.09.046.

Hubbert, M. K. (1937), Theory of scale models as applied to the study of geologic structures, *Bulletin of the Geological Society of America*, *48*, 1459–1520.

Klinkmüller, M., G. Schreurs, M. Rosenau, and H. Kemnitz (2016), Properties of granular analogue model materials: A community wide survey, *Tectonophysics*, *684*, 23–38, doi: 10.1016/j.tecto.2016.01.017.

Lockner, D. A., J. D. Byerlee, V. Kuksenko, A. Ponomarev, and A. Sidorin (1991), Quasi-Static Fault Growth and Shear Fracture Energy in Granite, *Nature*, *350*(6313), 39–42, doi:Doi 10.1038/350039a0.

Lohrmann, J., N. Kukowski, J. Adam, and O. Oncken (2003), The impact of analogue material properties on the geometry, kinematics, and dynamics of convergent sand wedges, *Journal of Structural Geology*, *25*(10), 1691–1711, doi:10.1016/S0191-8141(03)00005-1.

Masek, J. G., and C. C. Duncan (1998), Minimum-work mountain building, *Journal of Geophysical Research: Solid Earth*, *103*(B1), 907–917, doi:10.1029/97JB03213.

McLeod, A. E., N. H. Dawers, and J. R. Underhill (2000), The propagation and linkage of normal faults: insights from the Strathspey-Brent-Statfjord fault array, northern North Sea, *Basin Research*, *12*(3-4), 263–284, doi:10.1046/j.1365-2117.2000.00124.x.

Mitra, G., and S. E. Boyer (1986), Energy balance and deformation mechanisms of duplexes, *Journal of Structural Geology*, *8*(3-4), 291–304, doi:10.1016/0191-8141(86)90050-7.

Mouslopoulou, V., A. Nicol, T. Little, and J. Walsh (2007), Displacement transfer between intersecting regional strike-slip and extensional fault systems, *Journal of Structural Geology*, *29*(1), 100–116, doi:10.1016/j.jsg.2006.08.002.

Oncken, O., D. Boutelier, G. Dresen, and K. Schemmann (2012), Strain accumulation controls failure of a plate boundary zone: Linking deformation of the Central Andes and lithosphere mechanics, *Geochemistry, Geophysics, Geosystems*, *13*(12), doi: 10.1029/2012GC004280.

Otsu, N. (1979), A Threshold Selection Method from Gray-Level Histograms, *IEEE Transactions on Systems, Man, and Cybernetics*, *9*(1), 62–66, doi: 10.1109/TSMC.1979.4310076.

Panien, M., G. Schreurs, and O. A. Pfiffner (2006), Mechanical behaviour of granular materials used in analogue modelling: insights from grain characterisation, ring-shear tests and analogue experiments, *Journal of Structural Geology*, *28*(9), 1710–1724, doi: 10.1016/j.jsg.2006.05.004.

Paterson, M. S., and T.-f. Wong (2004), *Rock Deformation âĂŞ The Brittle Field*, 2 ed., 347 pp., Springer-Verlag, Berlin, Heidelberg.

Ramsay, J. (1980), Shear zone geometry: A review, *Journal of Structural Geology*, *2*(1-2), 83–99, doi:10.1016/0191-8141(80)90038-3.

Rechenmacher, A. L. (2006), Grain-scale processes governing shear band initiation and evolution in sands, *Journal of the Mechanics and Physics of Solids*, *54*(1), 22–45, doi: 10.1016/j.jmps.2005.08.009.

Ritter, M. C., K. Leever, M. Rosenau, and O. Oncken (2016), Scaling the sandbox – Mechanical (dis) similarities of granular materials and brittle rock, *Journal of Geophysical Research: Solid Earth*, *121*(9), 6863–6879, doi:10.1002/2016JB012915.

Ritter, M. C., T. Santimano, M. Rosenau, K. Leever, and O. Oncken (2017a), Co-Evolution of Stress and Strain in Riedel– and Critical Wedge–Experiments, *Tectonophysics*, *in review*.

Ritter, M. C., M. Rosenau, and O. Oncken (2017b), Supplement to: Growing Faults in the Lab: Insights into the Scale Dependence of the Fault Zone Evolution Process, *GFZ Data Service*, *in press*.

Rosenau, M., F. Corbi, and S. Dominguez (2017), Analogue earthquakes and seismic cycles: experimental modelling across timescales, *Solid Earth*, *8*(3), 597–635, doi: 10.5194/se-8-597-2017.

Scholz, C. H. (1987), Wear and gouge formation in brittle faulting, *Geology*, *15*(6), 493, doi:10.1130/0091-7613(1987)15<493:WAGFIB>2.0.CO;2.

Scholz, C. H. (2002), *The Mechanics of Earthquakes and Faulting*, 2nd editio ed., 471 pp., Cambridge University Press, Cambridge.

Scholz, C. H., and P. A. Cowie (1990), Determination of total strain from faulting using slip measurements, *Nature*, *346*(6287), 837–839, doi:10.1038/346837a0.

Schulze, D. (1994), Development and application of a Novel Ring Shear Tester, *Aufbereitungstechnik*, *35*(10), 524–535.

Tordesillas, A., and M. Muthuswamy (2009), On the modeling of confined buckling of force chains, *Journal of the Mechanics and Physics of Solids*, *57*(4), 706–727, doi: 10.1016/j.jmps.2009.01.005.

Wilson, B., T. Dewers, Z. Reches, and J. Brune (2005), Particle size and energetics of gouge from earthquake rupture zones, *Nature*, *434*(7034), 749–752, doi: 10.1038/nature03433.

Wong, T.-f. (1982), Shear fracture energy of Westerly granite from post-failure behavior, *Journal of Geophysical Research: Solid Earth*, *87*(B2), 990–1000, doi:

706   10.1029/JB087iB02p00990.